Research Square

Preprints are preliminary reports that have not undergone peer review.
They should not be considered conclusive, used to inform clinical practice,
or referenced by the media as validated information.

Closing the reaction-to-process loop with knowledge-intensified AI

Xiaonan Wang

wangxiaonan@tsinghua.edu.cn

Tsinghua University https://orcid.org/0000-0001-9775-2417

Zemeng Wang

Tsinghua University

Tian Yang

Tsinghua University https://orcid.org/0000-0002-7254-2584

Wentao Li

Tsinghua University

Ruixuan Chen

Tsinghua University

Kai Zhao

Tsinghua University

Jiangjie Qiu

Tsinghua University

Manu Suvarna

University of Greifswald

Zhuo Chen

Tsinghua University

Jianhong Xu

Tsinghua university https://orcid.org/0000-0002-3550-1345

Article

Keywords:

Posted Date: November 10th, 2026

DOI: https://doi.org/10.21203/rs.3.rs-11484464/v1

License: This work is licensed under a Creative Commons Attribution 4.0 International License.
Read Full License

Additional Declarations: There is **NO** Competing Interest.

Closing the reaction-to-process loop with knowledge-intensified AI

Zemeng Wang[1†], Tian Yang[2†], Wentao Li[1†], Ruixuan Chen[1], Kai Zhao[1], Jiangjie Qiu[1], Manu Suvarna[3], Zhuo Chen[2*], Jianhong Xu[2*], Xiaonan Wang[1*]

Affiliations:

[1] Beijing Key Laboratory of Artificial Intelligence for Advanced Chemical Engineering Materials, State Key Laboratory of Chemical Engineering and Low-Carbon Technology, Department of Chemical Engineering, Tsinghua University, Beijing 100084, China.

[2] State Key Laboratory of Chemical Engineering and Low-Carbon Technology, Department of Chemical Engineering, Tsinghua University, Beijing 100084, China.

[3] Department of Biotechnology & Enzyme Catalysis, Institute of Biochemistry, University of Greifswald, Greifswald 17487, Germany.

[†] These authors contributed equally to this work: Zemeng Wang, Tian Yang and Wentao Li.

*Corresponding authors. Email: wangxiaonan@tsinghua.edu.cn (Xiaonan Wang); xujianhong@tsinghua.edu.cn (Jianhong Xu); chenz2022@tsinghua.edu.cn (Zhuo Chen).

Abstract: Fine-chemical synthesis is extensively documented, yet kinetic and engineering knowledge for safe operation and scale-up remains scarce. Automated experiments supply additional data without necessarily yielding reusable process knowledge. We develop a knowledge-intensified closed loop (KI-cLoop) integrating chemical knowledge, automated continuous-flow experiments and physics-informed modelling. Its foundation, the Chemical World Skeleton Knowledge Graph (CWSKG), comprises approximately 3.6 million entities and 22 million relations across materials, reactions and processes. CWSKG organizes traceable evidence, experiments generate time-resolved data, an experimentally validated hybrid PINN–ODE model infers kinetics, and reactor models constrain scale-up. Across four strongly exothermic, data-scarce organic peroxide synthesis routes, kinetic fits ($R^2 > 0.92$) guided optimization considering yield, selectivity and conversion. Screening predicted a 17.8% relative yield improvement over the best measured yield for one route. Reactor simulations identified a heat-transfer-constrained scale-up boundary with net single-tube production approximately 126 times that of the reference tube. These outputs enrich CWSKG, advancing reaction records into experimentally supported, physically interpretable, scale-dependent process knowledge.

Main

Fine-chemical process development is complicated by hazardous reaction conditions and the diversity of products, routes, and operating parameters[1,2]. Hazardous conditions constrain systematic experimentation, while this diversity expands the process space beyond what conventional human-led experimentation can efficiently cover. This creates a pronounced knowledge imbalance, with abundant information on products and synthesis routes but comparatively limited time-resolved data and validated kinetic, mechanistic, operating, and scale-dependent knowledge. Once established, such process knowledge can be transferred across related reaction systems to accelerate new process development. Without such knowledge, translating reaction feasibility into safe operation and scale-up remains challenging[3]. Organic peroxides exemplify these challenges. They are widely used as free-radical initiators and curing agents[4], yet their synthesis often involves strongly exothermic reactions and thermally sensitive products[5,6]. Organic peroxides were involved in 12 of 167 serious reactive incidents analyzed by the U.S. Chemical Safety Board[7], while a recent peroxide runaway caused 10 fatalities and 110 injuries[8]. Addressing this knowledge imbalance requires progressively transforming reaction records into richer, experimentally supported, and reusable process knowledge for safe operation and scale-up.

Automated experimentation and continuous-flow platforms provide an important route to alleviate this data scarcity[9–12]. By enabling controlled and reproducible experimentation with reduced material hold-up and operator exposure, these platforms can systematically explore operating conditions for safety-sensitive systems[13–15]. However, many existing closed-loop experimental workflows remain primarily optimization-oriented. Measurements are used to identify improved yields, selectivities, or operating conditions[16,17], but such optimization does not by itself ensure that the generated data become reusable kinetic and engineering knowledge. Such knowledge is essential for understanding reaction rates and competition, predicting the effects of changing operating conditions[18,19], and assessing heat- and mass-transfer constraints during reactor scale-up[3,20], enabling experimental findings to support process analysis and decisions beyond individual condition-optimization campaigns[21]. The central challenge is therefore not merely to automate data generation, but to systematically integrate heterogeneous reaction data, capture shared knowledge across related reaction systems, and automate its transformation into physically interpretable and transferable process knowledge.

These heterogeneous reaction data are interconnected through shared chemical species, functional groups and related chemical transformations. Chemical knowledge graphs therefore provide a structured framework for representing these relationships and organizing the data for retrieval and reuse[22,23]. By linking materials, reactions, properties, operating conditions, and provenance, they enable fragmented information from literature, databases, and experiments to be represented in a connected and traceable form[24–26]. However, existing chemical and materials knowledge graphs can inherit the imbalance of the underlying chemical literature. Reported compounds, properties, and synthesis routes are abundant, whereas systematic experimental datasets and validated kinetic, mechanistic, and reactor-scale knowledge remain comparatively sparse. This limitation is compounded by the static nature of current knowledge graphs, while process development continuously generates new experimental evidence, inferred physical parameters, model assumptions, and scale-dependent constraints. A process-oriented chemical knowledge graph should therefore support updates to process knowledge while retaining its provenance and applicability conditions[27,28]. Within a closed-loop workflow, this evolving representation allows process knowledge generated by experiments and physical models to be progressively incorporated and retrieved to support subsequent development cycles.

In this work, we establish a knowledge-intensified closed loop (KI-cLoop; Fig. 1) that progressively transforms reaction records into experimentally supported and engineering-relevant process knowledge. The Chemical World Skeleton Knowledge Graph (CWSKG) provides the structured knowledge backbone, linking chemical species, reactions, operating conditions, physical quantities, and provenance. Graph-organized knowledge is retrieved and screened to identify executable route hypotheses, which are translated into automated continuous-flow experiments to generate time-resolved concentration data. We applied an experimentally validated hybrid physics-informed neural network–ordinary differential equation (PINN–ODE) model to four safety-sensitive, data-scarce organic peroxide synthesis routes, inferring kinetic parameters from 360 nonzero-time experimental observations and 60 calculated inlet states. The resulting models achieved product-concentration R^2 values of 0.928–0.992 and predicted a 17.8% relative yield improvement over the best measured yield for Route 1. Fitted kinetic parameters were further used in reactor-scale simulations coupling reaction and transport to identify a heat-transfer-constrained scale-up boundary. At this boundary, simulated net single-tube tert-butyl hydroperoxide (TBHP) production was approximately 126 times that of the reference tube. Experimental evidence, kinetic descriptions, operating recommendations and scale-up constraints were written back to CWSKG, allowing the knowledge base to evolve alongside process development. By enabling physically interpretable process knowledge to accumulate and be reused across reaction systems and scales, KI-cLoop could support the development and updating of process digital twins and coordinated decisions between experimental exploration and engineering design.

Results

Structuring sparse reaction and process knowledge

Turning sparse reaction records into reusable process knowledge requires a structured representation that connects chemical entities with experimental observations and physical quantities. Some existing materials knowledge graphs organize knowledge within specific material classes, such as zeolites[29]. Here, we constructed CWSKG as a foundational knowledge graph serving as a chemical world skeleton, connecting knowledge across material classes with experimental, kinetic and reactor-scale evidence (Fig. 2). The current CWSKG contains approximately 3.6 million entities and 22 million relations, spanning organic small molecules, inorganic solids, polymers, hybrid materials, catalysts, reaction species, and process-relevant records. These data are integrated from open-access databases, scientific literature, patents, computational studies, and experimental measurements. Within the organic-reaction subgraph, blue circles highlight regions with sparse or incomplete reaction data (Fig. 2a).

Organic reactions constitute an important component of CWSKG because they connect molecular entities to synthetic routes and, ultimately, to executable process decisions. However, the organic-reaction subgraph is unevenly populated. In sparse regions, a reported transformation may be linked to reactants and products but lack time-resolved concentration data, catalyst-dependent behavior, validated operating windows, side-reaction information, or scale-dependent thermal constraints (Fig. 2b). Such incompleteness limits the direct use of reaction records for route selection, as a chemically plausible route is not necessarily experimentally executable or engineering-feasible.

CWSKG addresses this limitation through a dual-dimensional architecture that jointly represents material entities and embedded physical quantities (Fig. 2c). The material dimension organizes species and process-relevant entities, including reactants, products, catalysts, solvents, routes, and applications. The physical-quantity dimension organizes thermodynamic, kinetic, and process descriptors, including Gibbs free energy, enthalpy, entropy, activation energy, rate constants, reaction orders, reaction rates, and operating variables. Inter-layer bridge relations explicitly associate a material, reaction, or route with its measured or inferred quantities, together with their provenance and confidence.

Through this architecture, retrieving a route can also reveal its evidential status by identifying reported conditions, measured or inferred kinetic quantities, conflicting values, and process constraints that remain unavailable. Conversely, outputs generated in the KI-cLoop, including concentration–time profiles from automated experiments, route-specific kinetic parameters from physics-informed inference, and thermal and scale-up constraints from reactor simulation, can be attached to the same route context. Thus, the dual-dimensional representation provides a structured path for transforming a sparsely documented reaction record into progressively richer and traceable process knowledge.

Traceable retrieval of executable peroxide routes

Building on the CWSKG, we developed a graph-based retrieval-augmented generation (RAG) workflow for chemical material and process questions (Fig. 3)[30,31]. For a user query, the system retrieves relevant nodes, attributes, and relations, assembles them into a structured node context, and supplies this context to a large language model for generating answers[32,33]. In the organic peroxide case study, the system was queried to identify which organic peroxides can serve as

oxidizers or radical initiators and to retrieve available synthesis pathways and process conditions for their preparation.

The retrieval process jointly uses node and edge attributes. Therefore, the resulting context can link material entities with synthesis routes, reactants, solvents, operating conditions, procedural information, and safety-relevant attributes. This graph-structured context enables simultaneous consideration of multiple constraints during route screening, including target function, route availability, reported performance, reagent accessibility, experimental compatibility, and safety-related factors such as hazardous functionalities, operating conditions, and process limitations.

The initial retrieval returned a chemically diverse set of organic peroxide candidates and synthesis records (Supplementary Fig. 5). This diversity included routes accessing the same target peroxide through different starting materials and catalytic environments, as well as routes producing structurally distinct peroxide products. The retrieved evidence was subsequently narrowed to four routes for experimental validation: Route 1, TBHP formation from tert-butyl chloride (TBCL) and H_2O_2; Route 2, TBHP formation from tert-butanol (TBA) and H_2O_2 using phosphotungstic-acid catalysis; Route 3, TBHP formation from tert-butanol and H_2O_2 using trifluoroacetic-acid catalysis; and Route 4, tert-butyl peroxybenzoate (TBPB) formation from benzaldehyde and TBHP in a tetrabutylammonium iodide (TBAI)/acetonitrile system.

Beyond route retrieval, graph-based RAG supports chemical-material and process questions using graph-grounded context. These include material identities and functions, associated properties, reaction relationships, synthetic accessibility and reported operating conditions. In the 120-question benchmark constructed for this study, the knowledge-intensified (KI) system, comprising a local Qwen2-7B-Instruct model, graph retrieval and numerical tools, achieved a mean task-completion score of 79.8/100, compared with 46.9–48.2 for four general-purpose language models. On project-dependent questions (Q2–Q6), the KI system scored 80.50/100, compared with 36.63–38.13/100 for the general models, a difference of 42.4–43.9 points. These results show that the KI system can use accumulated reaction and process evidence to outperform general-purpose models in quantitative analysis and process interpretation (Supplementary Fig. 7; Supplementary Table 10).

Overall, the graph-based RAG workflow proceeds from graph search to node retrieval, pathway tracing, and candidate route screening. This stage yields a set of traceable, experimentally executable route hypotheses to guide subsequent automated experiments.

Automated flow validation of peroxide synthesis routes

We combined modular automation[34] and microreactor technology[35] to implement the four graph-selected peroxide routes on an automated flow platform comprising feed preparation, route switching, reagent delivery, microreaction, quenching, sample preparation, high-performance liquid chromatography (HPLC) analysis and robot-assisted handling (Fig. 3). Automation enabled the systematic execution of route-specific condition combinations while maintaining a common analytical workflow across chemically distinct reactions[36]. The campaigns generated 60 route–condition families and 420 processed concentration states, comprising 60 calculated inlet states and 360 nonzero-time observations, providing a consistent experimental basis for comparing the four routes. Record counts are summarized in Supplementary Table 11.

The condition space was specified separately for each route according to its reactants and catalytic system. Route 1 comprised 13 condition families, spanning 30–60 °C and H_2O_2/TBCL feed ratios

of 1.0–6.0. Route 2 comprised 15 condition families, spanning 60–80 °C, H_2O_2/TBA feed ratios of 1.2–2.2, and phosphotungstic acid concentrations of 0.047–0.165 mol l^{-1}. Route 3 comprised 17 condition families, spanning 60–85 °C, H_2O_2/TBA feed ratios of 1.2–2.0, and trifluoroacetic acid concentrations of 1.424–3.213 mol l^{-1}. Route 4 comprised 15 condition families, spanning 45–65 °C, with route-specific variations in benzaldehyde, TBHP, and TBAI concentrations. Complete condition matrices, yield trajectories and species-resolved states are provided in Supplementary Information, sections S5.1–S5.4.

Each condition family contains one inlet state calculated from feed composition and flow rates and six nonzero-time observations. The non-zero sampling windows were 1.03–28.86 min for Route 1, 0.67–28.62 min for Routes 2 and 3, and 0.88–24.74 min for Route 4. The dataset contains 91, 105, 119, and 105 processed states for Routes 1–4, respectively, including 13, 15, 17, and 15 calculated inlet states.

The measured profiles revealed distinct experimental characteristics for the four routes (Fig. 4a, b). Route 1 proceeded without an added catalyst and showed gradual TBHP accumulation over the sampled window. Its best measured TBHP yield was 0.439. Routes 2 and 3 both produced TBHP from tert-butanol and H_2O_2 but required different acidic catalytic environments and temperature ranges. Route 2 reached a best measured TBHP yield of 0.784 at 75 °C with a phosphotungstic acid concentration of 0.109 mol l^{-1}, whereas Route 3 reached 0.787 at 85 °C with a trifluoroacetic acid concentration of 2.721 mol l^{-1}. Both routes produced di-tert-butyl peroxide (DTBP) as a by-product. Route 4 reached a best measured product yield of 0.725 for TBPB at 60 °C using a TBHP/benzaldehyde ratio of 1.10 and a TBAI concentration of 0.311 mol l^{-1}.

The four routes exhibited distinct characteristics in terms of yield, catalyst requirement, and selectivity. Route 1 proceeded without an added catalyst but gave a lower final TBHP yield and required excess H_2O_2. Routes 2 and 3 achieved comparable TBHP yields under different acidic catalytic environments. Route 2 used phosphotungstic-acid catalysis and gave its best experimental result at 75 °C, whereas Route 3 used trifluoroacetic acid and reached its best experimental performance at a higher temperature of 85 °C. Both routes produced DTBP as a side product. Route 4 used TBHP as a reactant to form TBPB and reached its best experimental product yield at 60 °C. Condition-level yield distributions and TBHP–DTBP selectivity trajectories are shown in Supplementary Figs. 40 and 41.

Route-specific kinetics and operating optima

Organic peroxide synthesis is safety-sensitive and often supported by limited process data. Graph-retrieved evidence and automated concentration profiles alone cannot explain how temperature, catalyst loading, reactant ratio, and competing reactions affect reaction behavior. To interpret the differences observed among the four routes, we used mechanism-informed kinetic modeling to translate the time-resolved data into route-specific kinetic descriptions.

We first assessed the reliability of the hybrid PINN–ODE model using a separate Paal–Knorr experimental dataset. The final apparent activation energy was 12.3 kJ mol^{-1}, numerically close to the 12.2 ± 0.4 kJ mol^{-1} reported by Moore and Jensen for the first step of their two-step model[37]. Differences in kinetic models and experimental conditions limit this comparison to a check on kinetic plausibility. The kinetic assessment is detailed in Supplementary Information, section S4.

The same hybrid PINN–ODE model was then fitted separately to each peroxide route, with the assumed rate-law structure embedded directly in the concentration-profile fitting procedure[38–40].

The resulting product predictions agreed closely with the measured data, giving product R^2 values of 0.986, 0.989, 0.992, and 0.928 for Routes 1–4, respectively (Fig. 4c). The corresponding product mean absolute errors ranged from 0.035 to 0.061 mol l^{-1}. These results quantify agreement for the assumed rate laws. The rate laws, fitted parameters and fit/validation metrics are provided in Supplementary Tables 22 and 24.

The fitted kinetic descriptions distinguished the reaction characteristics of the four routes (Fig. 4d). Route 1 was represented by a single TBHP formation step. For Routes 2 and 3, the rate expressions explicitly included TBHP formation, along with the competing conversion of tert-butanol and TBHP to DTBP. Route 2 and Route 3 showed different apparent dependencies on their respective acidic catalysts and distinct main- and side-reaction activation terms. Route 4 was described by TBPB formation from benzaldehyde and TBHP. The fitted main-reaction apparent activation energies were 9.07, 101.14, 123.43, and 4.49 kJ mol^{-1} for Routes 1–4.

The four peroxide kinetic models were used to explore previously untested combinations of feed ratio, catalyst concentration, temperature and residence time for each route. Within the sampled marginal ranges, model-guided screening predicted relative yield gains of 17.8% and 0.9% over the best measured yields for Routes 1 and 4, respectively. For Routes 2 and 3, conditions selected by the joint yield–selectivity–conversion objective gave predicted TBHP selectivities of 86.6% and 89.3%, respectively. We evaluated the four routes across five criteria: yield, selectivity, productivity, kinetic accessibility and greenness. Route 3 offered the highest productivity, predicted product yield and overall score, whereas Route 2 had the lowest estimated global warming potential (GWP). The screened conditions are listed in Supplementary Table 23.

Heat-transfer constraints on reactor scale-up

Kinetic analysis provides reaction-condition recommendations and a basis for assessing how production can be scaled up under reactor-scale heat-transfer constraints[20,41,42]. Therefore, we selected Route 2, the phosphotungstic-acid-catalyzed synthesis of TBHP, as a representative engineering case and coupled the fitted Route 2 kinetic parameters with a two-dimensional axisymmetric tubular-reactor model in COMSOL Multiphysics (Fig. 5).

Laboratory-scale reaction performance cannot be directly transferred to a larger reactor. Increasing the tube radius increases both the reaction volume and heat generation, but decreases the wall area available for heat removal per unit reactor volume. This imbalance may lead to local temperature rises that reduce the reaction yield. Considering the exothermic oxygen-evolving decomposition of H_2O_2, the thermal instability of organic peroxides, and the potential for tert-butanol volatilization and pressure increase at elevated temperatures, 368 K was selected as the engineering thermal-screening limit for the reactor simulation.

The model coupled laminar flow, mass transport, and heat transfer, with the reaction-rate and heat-generation terms determined from the fitted Route 2 kinetic parameters and reaction enthalpy. The reactor length and inlet conditions were fixed, while the tube radius was scanned from 1 to 20 mm to identify the largest single-tube radius compatible with the thermal criterion. At a radius of 8 mm, the calculated maximum temperature was 366.712 K and the flux-based net outlet TBHP yield was 45.02%. Net single-tube TBHP production increased approximately 126-fold relative to the 1 mm-radius reference tube. When the radius was increased to 9 mm, the maximum temperature increased to 368.055 K and exceeded the predefined thermal-screening limit. Screened-radius

performance and the production-gain calculation are provided in Supplementary Table 29 and Supplementary Information, section S7.4.

Under the current model and design criterion, a radius of 8 mm (diameter 16 mm) represents the largest feasible single-tube design. Further capacity expansion should consider the parallel operation of microreactors that satisfy the thermal constraint through numbering-up[43]. This analysis translates route-specific kinetic knowledge into reactor design constraints and provides an engineering basis for connecting laboratory reaction data with scale-up decisions. The experimental and modeling outputs were written back to the CWSKG and subsequently retrieved for reuse in 13 illustrative cases covering kinetic interpretation, condition recommendations, route evaluation, reactor sizing and the screening of related reactions (Supplementary Table 30; Supplementary Data). These cases illustrate how newly generated process knowledge can support subsequent analysis and experimental planning.

Discussion

In this work, we establish KI-cLoop to connect reaction evidence with the kinetic and reactor-scale knowledge needed for process development. The framework integrates the Chemical World Skeleton Knowledge Graph (CWSKG), traceable route retrieval, automated continuous-flow experimentation, physics-informed kinetic inference and reactor modeling. Across four organic peroxide routes, 360 nonzero-time observations and 60 calculated inlet states supported route-specific kinetic descriptions with product R^2 values of 0.928–0.992 for the fitted data, enabling interpretation of competing reactions and comparison of operating conditions. The resulting kinetic models supported condition screening that balanced yield, selectivity and conversion, identifying opportunities to improve overall reaction performance. The reactor-scale heat-transfer analysis identified a thermal-screening boundary for single-tube enlargement, with an approximately 126-fold simulated production increase relative to the reference tube. These results demonstrate a progression from reported reaction feasibility to experimentally supported kinetic knowledge and engineering constraints.

Existing automated reaction-development workflows have advanced condition optimization, while chemical knowledge graphs and mechanistic modeling provide complementary capabilities for organizing evidence and predicting process behavior. A remaining challenge is to connect these capabilities so that experimental findings become reusable kinetic and engineering knowledge with traceable provenance and clear applicability limits. KI-cLoop addresses this gap by linking route retrieval, experimentation, model inference and knowledge writeback within a common route context. Graph retrieval supplies traceable evidence, automated flow experiments generate time-resolved data, and kinetic models quantify reaction sensitivities and competition. Reactor analysis extends these descriptions to transport and thermal constraints. Organic peroxide synthesis presents substantial thermal risks[44]. For the routes examined here, limited kinetic data make these connections particularly important. We combined automated flow experiments with physics-informed modeling to obtain route-specific kinetic parameters and used reactor analysis to assess thermal constraints on scale-up. The resulting thermal-screening boundary supports consideration of numbering-up, subject to validation of the reactor and safety assumptions[3,43]. Autonomous molecular-discovery platforms have demonstrated how experimental feedback can update predictive models and guide subsequent exploration[45]. Writing the resulting concentration profiles, kinetic parameters, operating recommendations and engineering constraints back to their originating routes allows CWSKG to evolve as evidence accumulates. This accumulated knowledge supports subsequent interpretation, reaction screening and engineering assessment, connecting individual investigations to continued process development.

Integrating AI with traceable experimental evidence and physical models offers a path toward chemical manufacturing that learns systematically from accumulated process knowledge. Realizing this prospect requires broader validation beyond the four liquid-phase peroxide synthesis routes examined here. Future work should acquire experimental data across different phases and refine the corresponding reaction and transport models to extend the framework to solid-state, gas-phase and multiphase systems, enabling accumulated and experimentally validated process knowledge to support a wider range of experimental designs and process decisions. By supporting the accumulation and reuse of physically interpretable knowledge across reaction systems and scales, KI-cLoop could provide an evolving knowledge foundation for process digital twins and coordinated experimental and engineering decisions.

Methods

CWSKG construction and graph retrieval

The Chemical World Skeleton Knowledge Graph (CWSKG) was constructed as the evidence backbone of the KI-cLoop by integrating chemical and process information from open-access databases, patent records, scientific literature, computational studies, and laboratory measurements. Major structured sources included the United States Patent and Trademark Office (USPTO) reaction dataset[46], the Computation-Ready, Experimental Metal–Organic Framework (CoRE MOF) database[47], the Materials Project[48], Catalysis-Hub[49], the Open Catalyst Project[50], the Quantum MOF (QMOF) database[51], and the Clean Energy Project Database (CEPDB)[52], together with computational and experimental data generated within our study. Public reference releases and access links are listed in Supplementary Tables 3 and 4. The metadata schema is specified in Supplementary Information, section S1.2.

The reaction-space visualization in Fig. 2 was inspired by the fingerprint-based reaction atlases of Schwaller et al[53]. We constructed the present map from reaction-center descriptors using unsupervised t-distributed stochastic neighbor embedding (t-SNE)[54]. Data selection, classification and projection method[55] are described in Supplementary Information, section S1.3.

Unstructured literature and patent records were converted into graph-ready information using ontology-informed large language model-assisted extraction[56]. Domain-adapted prompts were used to identify chemical entities, material properties, synthesis procedures, operating conditions, and typed relationships. The extracted records retained the source, version, and confidence metadata, and representative records were manually reviewed for quality control. The extraction workflow and record structure are illustrated in Supplementary Figs. 3 and 4 (Supplementary Information, section S1.4).

CWSKG uses a dual-dimensional representation comprising a material dimension and a physical-quantity dimension. The material dimension represents chemical species, material classes, reactants, products, catalysts, solvents, reaction routes, and applications. The physical-quantity dimension represents thermodynamic, kinetic, and process descriptors, including enthalpy, activation energy, rate constants, reaction orders, reaction rates, and operating variables. Bridge relations connect material or reaction records with measured or inferred physical quantities while retaining their provenance and confidence. The current graph contains approximately 3.6 million entities and 22 million relations (Supplementary Tables 31 and 32).

For retrieval, each graph node was represented by a unique node identity and a structured node context containing node attributes and relation-derived information from neighboring entities. Query-relevant nodes and contexts were retrieved by semantic matching, after which graph traversal and pathway tracing were used to assemble connected reaction evidence. In the peroxide case study, candidate routes were screened according to target relevance, literature maturity, mechanistic plausibility, reagent accessibility, safety considerations, reported reaction performance, and compatibility with the automated flow platform. Four routes were retained for experimental investigation. The retrieval workflow and its configuration are described in Supplementary Information, section S2.2.

Processed experimental records, fitted kinetics, screened conditions and reactor simulation results were written back to the CWSKG as records linked to their respective reaction routes, together with their sources, units and applicability limits (Supplementary Information, section S8). These additions progressively enrich the graph and enable it to evolve as process knowledge accumulates.

The evolving graph supports retrieval-augmented generation to inform subsequent experimental design and scale-up analysis. We developed 13 illustrative cases to demonstrate the reuse of this accumulated knowledge (Supplementary Information, section S8.1).

Question-answering evaluation

We evaluated the KI system against the representative large language models including GPT-5.6 Sol, Qwen3.8-Max, DeepSeek-V4-Pro-0813 and GLM-5.3 on 120 questions across six categories (20 per category). The KI system combined Qwen2-7B-Instruct with graph retrieval and numerical tools. The general-purpose models were evaluated using the same questions and response instructions. Two large language model evaluators, GPT-5.6 Sol and GLM-5.3, scored the responses[57]. Evaluation methods and aggregate results are described in Supplementary Information, sections S2.3–S2.4. The 120 questions and scientific reference answers are provided in Supplementary Data.

Automated flow experiments

Four graph-selected organic peroxide routes were investigated using a modular automated flow platform comprising reagent preparation, route switching, reagent delivery, microreaction, quenching, sample preparation, chromatographic analysis, and robot-assisted handling. The platform was used to execute route-specific combinations of temperature, feed composition, and catalyst or acid concentration while maintaining a common sampling and analytical workflow.

Route 1 comprised TBHP formation from tert-butyl chloride and H_2O_2. Thirteen condition families were investigated at 30–60 °C using H_2O_2/tert-butyl chloride feed ratios of 1.0–6.0. Route 2 comprised phosphotungstic-acid-catalyzed TBHP formation from tert-butanol and H_2O_2. Fifteen condition families were investigated at 60–80 °C using H_2O_2/tert-butanol ratios of 1.2–2.2 and phosphotungstic acid concentrations of 0.047–0.165 mol l^{-1}. Route 3 comprised trifluoroacetic acid-catalyzed TBHP formation from tert-butanol and H_2O_2. Seventeen condition families were investigated at 60–85 °C using H_2O_2/tert-butanol ratios of 1.2–2.0 and trifluoroacetic acid concentrations of 1.424–3.213 mol l^{-1}. Route 4 comprised TBPB formation from benzaldehyde and TBHP in a TBAI/acetonitrile system. Fifteen condition families were investigated at 45–65 °C by varying benzaldehyde, TBHP, and TBAI concentrations (Supplementary Tables 12–15).

Each condition family included one inlet state calculated from feed composition and flow rates and six nonzero residence-time observations. The non-zero residence-time ranges were 1.03–28.86 min for Route 1, 0.67–28.62 min for Routes 2 and 3, and 0.88–24.74 min for Route 4. In total, 60 route–condition families provided 420 processed concentration states: 91, 105, 119, and 105 for Routes 1–4, respectively. The 360 non-initial observations were used for kinetic fitting, and the inlet states specified the boundary conditions.

Samples were quenched and analyzed by HPLC to obtain the concentrations of the species represented in the route-specific kinetic models, including DTBP for Routes 2 and 3. Concentration processing, response factors and platform operation are described in Supplementary Information, sections S3.2–S3.5.

Kinetic modeling and condition search

Kinetic inference was performed separately for each route using a hybrid PINN–ODE model. First, an ODE model was fitted to the experimental data to obtain initial kinetic parameters, and its predicted concentration profiles were used to pretrain the neural network. The network and kinetic parameters were then jointly optimized using the experimental data, ODE predictions and reaction-kinetic constraints. Details are provided in Supplementary Information, sections S4.1 and S6.3.

Temperature dependence was represented using an Arrhenius-type expression[58],

$$k_j = A_j \exp\left(-\frac{E_{a,j}}{RT}\right) \qquad (1)$$

where k_j is the rate coefficient for reaction j, A_j is the pre-exponential factor, $E_{a,j}$ is the apparent activation energy, R is the gas constant, and T is the absolute temperature[59]. For catalyst- or acid-dependent reactions, the corresponding concentration dependence was incorporated into an apparent condition-dependent rate coefficient,

$$k_j^* = A_j C_{\mathrm{cat}}^{\eta_j} \exp\left(-\frac{E_{a,j}}{RT}\right) \qquad (2)$$

where C_{cat} denotes the phosphotungstic acid, trifluoroacetic acid, or TBAI concentration, as applicable, and η_j is the fitted apparent reaction order with respect to the catalyst or acid.

For Route 1, TBHP formation from tert-butyl chloride (TBCL) and hydrogen peroxide was represented by a single reaction,

$$r_1 = k_1 C_{\mathrm{H_2O_2}}^{\alpha_1} C_{\mathrm{TBCL}}^{\beta_1} \qquad (3)$$

with the corresponding material balances,

$$\frac{\mathrm{d}C_{\mathrm{H_2O_2}}}{\mathrm{d}t} = \frac{\mathrm{d}C_{\mathrm{TBCL}}}{\mathrm{d}t} = -r_1, \qquad \frac{\mathrm{d}C_{\mathrm{TBHP}}}{\mathrm{d}t} = r_1 \qquad (4)$$

For Routes 2 and 3, TBHP formation from tert-butanol (TBA) and hydrogen peroxide was coupled to the competing formation of di-tert-butyl peroxide (DTBP),

$$r_1 = k_1^* C_{\mathrm{H_2O_2}}^{\alpha_1} C_{\mathrm{TBA}}^{\beta_1} \qquad (5)$$

$$r_2 = k_2^* C_{\mathrm{TBA}}^{\alpha_2} C_{\mathrm{TBHP}}^{\beta_2} \qquad (6)$$

and the concentration profiles were obtained by integrating

$$\frac{\mathrm{d}C_{\mathrm{H_2O_2}}}{\mathrm{d}t} = -r_1, \qquad \frac{\mathrm{d}C_{\mathrm{TBA}}}{\mathrm{d}t} = -r_1 - r_2 \qquad (7)$$

$$\frac{\mathrm{d}C_{\mathrm{TBHP}}}{\mathrm{d}t} = r_1 - r_2, \qquad \frac{\mathrm{d}C_{\mathrm{DTBP}}}{\mathrm{d}t} = r_2 \qquad (8)$$

The phosphotungstic acid and trifluoroacetic acid systems were fitted independently, with separate main- and side-reaction kinetic parameters and route-specific apparent acid dependencies.

For Route 4, TBPB formation from benzaldehyde and TBHP in the presence of TBAI was represented as

$$r_1 = k_1^* C_{\mathrm{benzaldehyde}}^{\alpha_1} C_{\mathrm{TBHP}}^{\beta_1} \qquad (9)$$

with the material balances

$$\frac{\mathrm{d}C_{\mathrm{benzaldehyde}}}{\mathrm{d}t} = -r_1, \qquad \frac{\mathrm{d}C_{\mathrm{TBHP}}}{\mathrm{d}t} = -2r_1, \qquad \frac{\mathrm{d}C_{\mathrm{TBPB}}}{\mathrm{d}t} = r_1 \qquad (10)$$

The final kinetic parameters were inferred by minimizing a concentration least-squares objective over non-initial observations,

$$\boldsymbol{\theta}^* = \underset{\boldsymbol{\theta}}{\operatorname{argmin}} \left[\sum_{s=1}^{N_{\mathrm{sp}}} \sum_{i=1}^{N_s} \left(C_{s,i}^{\mathrm{pred}} - C_{s,i}^{\mathrm{exp}} \right)^2 \right] \qquad (11)$$

where N_{sp} is the number of fitted chemical species, N_s is the number of non-initial observations for species s, and $C_{s,i}^{\mathrm{pred}}$ and $C_{s,i}^{\mathrm{exp}}$ are the predicted and measured concentrations, respectively. The balance equations and final fitting objective are detailed in Supplementary Information, sections S4.1 and S6.1. For the Paal–Knorr benchmark, the inferred apparent activation energy was compared with the first-step value reported by Moore and Jensen[37]. Experimental procedures and kinetic assessment are provided in Supplementary Information, sections S3.6 and S4 (Supplementary Data).

Model agreement on non-initial observations was quantified using the coefficient of determination (R^2), mean absolute error (MAE) and mean squared error (MSE),

$$R^2 = 1 - \frac{\sum_i \left(C_i^{\mathrm{exp}} - C_i^{\mathrm{pred}} \right)^2}{\sum_i \left(C_i^{\mathrm{exp}} - \overline{C}^{\mathrm{exp}} \right)^2} \qquad (12)$$

$$\mathrm{MAE} = \frac{1}{N} \sum_i \left| C_i^{\mathrm{pred}} - C_i^{\mathrm{exp}} \right|, \qquad \mathrm{MSE} = \frac{1}{N} \sum_i \left(C_i^{\mathrm{pred}} - C_i^{\mathrm{exp}} \right)^2 \qquad (13)$$

The fitted models were subsequently used to search for route-specific operating conditions within the sampled marginal ranges. Observed discrete feed-ratio and catalyst or acid levels were recombined subject to the feed-mixing constraint and measured concentration ranges. Temperature was scanned in 1 °C steps, and residence time was screened at 241 points within the measured interval and subsequently refined. Yield was defined as

$$Y = \frac{C_{\mathrm{product}}}{\min\left(C_{\mathrm{reactant},1,0}, \nu^{-1} C_{\mathrm{reactant},2,0} \right)} \qquad (14)$$

where $\nu = 1$ for Routes 1-3 and $\nu = 2$ for Route 4. For Routes 2 and 3, TBHP selectivity was defined as

$$S_{\mathrm{TBHP}} = \frac{C_{\mathrm{TBHP}}}{C_{\mathrm{TBHP}} + C_{\mathrm{DTBP}}} \qquad (15)$$

Route-specific desirability functions were used solely to rank model-generated candidate conditions. Yield, selectivity and productivity definitions are given in Supplementary Information, section S6.2.

Route evaluation

The four routes were evaluated using five criteria: yield, selectivity, volumetric productivity, kinetic accessibility, and greenness. Yield was calculated as the target-product concentration divided by the stoichiometrically limiting initial reactant concentration, as defined in equation (14). Selectivity was defined using the route-specific product and by-product species represented in the kinetic model. Volumetric productivity was defined as the target-product concentration divided by the residence time. Kinetic accessibility was represented using the fitted apparent activation term of the main reaction, with lower activation terms assigned higher desirability.

Greenness was evaluated at the screened conditions using AI-assisted life cycle assessment[60,61]. Background data were obtained from the ecoinvent v3.10 and HiQLCD v1.2.0[62,63]. Environmental impacts were characterized using global warming potential, expressed as kg CO_2-equivalent per kg product. The resulting values were 5.075, 3.268, 3.468, and 12.303 for Routes 1–4, respectively. The evaluation assumed 95% recycling and 5% loss of unreacted recyclable materials. Recyclable catalysts were accounted for according to their assumed loss fractions, and by-product credits were applied where appropriate. The functional-unit assumptions, inventory factors and by-product-credit sensitivity are detailed in Supplementary Information, sections S7.1–S7.2.

Reactor modeling and scale-up

Reactor-scale analysis was performed for Route 2, the phosphotungstic-acid-catalyzed synthesis of TBHP from tert-butanol and H_2O_2. A two-dimensional axisymmetric tubular-reactor model was implemented in COMSOL Multiphysics by coupling laminar flow, species transport, and heat transfer. The reaction-rate and heat-generation terms use the Route 2 kinetic parameter set and reaction enthalpies.

Tube radius was varied at fixed reactor length, inlet conditions and cooling conditions. The largest tested radius satisfying a prescribed maximum-temperature constraint was selected, and further capacity expansion was estimated by numbering-up under identical flow and cooling conditions. Model geometry, governing equations and additional temperature profiles are provided in Supplementary Information, sections S7.3–S7.4.

Data availability

Experimental records, the 120 benchmark questions and scientific reference answers, and knowledge-reuse cases are provided in Supplementary Data. Processed kinetic data and model outputs are available at https://github.com/ColinWangZM/KI-cLoop-research.

Code availability

Code for knowledge graph construction and retrieval, hybrid PINN–ODE modeling and data analysis is available at https://github.com/ColinWangZM/KI-cLoop-research.

References

1. Dakkoune, A., Vernières-Hassimi, L., Leveneur, S., Lefebvre, D. & Estel, L. Analysis of thermal runaway events in French chemical industry. *J. Loss Prev. Process Ind.* **62**, 103938 (2019).

2. Khan, F. I. & Abbasi, S. A. Major accidents in process industries and an analysis of causes and consequences. *J. Loss Prev. Process Ind.* **12**, 361–378 (1999).

3. Stoessel, F. *Thermal Safety of Chemical Processes: Risk Assessment and Process Design*. (Wiley-VCH, Weinheim, 2008).

4. Yaremenko, I. A., Vil', V. A., Demchuk, D. V. & Terent'ev, A. O. Rearrangements of organic peroxides and related processes. *Beilstein J. Org. Chem.* **12**, 1647–1748 (2016).

5. Lv, J., Chen, W., Chen, L., Tian, Y. & Yan, J. Thermal risk evaluation on decomposition processes for four organic peroxides. *Thermochim. Acta* **589**, 11–18 (2014).

6. Gong, L.-Q., Li, L., Pan, Y., Jiang, J.-J. & Jiang, J.-C. Thermal hazards and initial decomposition mechanisms study of four tert-butyl organic peroxides combining experiments with density functional theory method. *Thermochim. Acta* **708**, 179142 (2022).

7. U.S. Chemical Safety and Hazard Investigation Board. *Improving Reactive Hazard Management*. https://www.csb.gov/assets/1/20/ReactiveHazardInvestigationReport.pdf (2002).

8. Huang, Z. *et al.* Identification of autocatalysis in organic peroxides. *ACS Chem. Health Saf.* **33**, 580–591 (2026).

9. Burger, B. *et al.* A mobile robotic chemist. *Nature* **583**, 237–241 (2020).

10. MacLeod, B. P. *et al.* Self-driving laboratory for accelerated discovery of thin-film materials. *Sci. Adv.* **6**, eaaz8867 (2020).

11. Häse, F., Roch, L. M. & Aspuru-Guzik, A. Next-generation experimentation with self-driving laboratories. *Trends Chem.* **1**, 282–291 (2019).

12. Tom, G. *et al.* Self-driving laboratories for chemistry and materials science. *Chem. Rev.* **124**, 9633–9732 (2024).

13. Plutschack, M. B., Pieber, B., Gilmore, K. & Seeberger, P. H. The hitchhiker's guide to flow chemistry. *Chem. Rev.* **117**, 11796–11893 (2017).

14. Gutmann, B., Cantillo, D. & Kappe, C. O. Continuous-flow technology—a tool for the safe manufacturing of active pharmaceutical ingredients. *Angew. Chem. Int. Ed.* **54**, 6688–6728 (2015).

15. Leong, S. X. *et al.* Steering towards safe self-driving laboratories. *Nat. Rev. Chem.* **9**, 707–722 (2025).

16. Bennett, J. A. *et al.* Autonomous reaction Pareto-front mapping with a self-driving catalysis laboratory. *Nat. Chem. Eng.* **1**, 240–250 (2024).

17. Shields, B. J. *et al.* Bayesian reaction optimization as a tool for chemical synthesis. *Nature* **590**, 89–96 (2021).

18. Hone, C. A., Holmes, N., Akien, G. R., Bourne, R. A. & Muller, F. L. Rapid multistep kinetic model generation from transient flow data. *React. Chem. Eng.* **2**, 103–108 (2017).

19. Ji, W. & Deng, S. Autonomous discovery of unknown reaction pathways from data by chemical reaction neural network. *J. Phys. Chem. A* **125**, 1082–1092 (2021).

20. Bird, R. B., Stewart, W. E. & Lightfoot, E. N. *Transport Phenomena*. (Wiley, New York, 2002).

21. Agunloye, E. *et al.* Automated kinetic model identification via cloud services using model-based design of experiments. *React. Chem. Eng.* **9**, 1859–1876 (2024).

22. Hogan, A. *et al.* Knowledge graphs. *ACM Comput. Surv.* **54**, 71 (2021).

23. Kearnes, S. M. *et al.* The Open Reaction Database. *J. Am. Chem. Soc.* **143**, 18820–18826 (2021).

24. Olivetti, E. A. *et al.* Data-driven materials research enabled by natural language processing and information extraction. *Appl. Phys. Rev.* **7**, 041317 (2020).

25. Venugopal, V. & Olivetti, E. MatKG: an autonomously generated knowledge graph in material science. *Sci. Data* **11**, 217 (2024).

26. Kononova, O. *et al.* Text-mined dataset of inorganic materials synthesis recipes. *Sci. Data* **6**, 203 (2019).

27. Wilkinson, M. D. *et al.* The FAIR Guiding Principles for scientific data management and stewardship. *Sci. Data* **3**, 160018 (2016).

28. Zhang, S., Zhang, J. & Lapkin, A. A. A knowledge graph framework for digital twins of chemical processes. *Nat. Chem. Eng.* **3**, 286–297 (2026).

29. Kondinski, A. *et al.* Knowledge graph representation of zeolitic crystalline materials. *Digit. Discov.* **3**, 2070–2084 (2024).

30. Lewis, P. *et al.* Retrieval-augmented generation for knowledge-intensive NLP tasks. in *Advances in Neural Information Processing Systems* (eds Larochelle, H., Ranzato, M., Hadsell, R., Balcan, M. F. & Lin, H.) vol. 33 9459–9474 (Curran Associates, Inc., 2020).

31. He, X. *et al.* G-Retriever: retrieval-augmented generation for textual graph understanding and question answering. in *Advances in Neural Information Processing Systems* (eds Globerson, A. et al.) vol. 37 132876–132907 (Curran Associates, Inc., 2024).

32. M. Bran, A. *et al.* Augmenting large language models with chemistry tools. *Nat. Mach. Intell.* **6**, 525–535 (2024).

33. Boiko, D. A., MacKnight, R., Kline, B. & Gomes, G. Autonomous chemical research with large language models. *Nature* **624**, 570–578 (2023).

34. Steiner, S. *et al.* Organic synthesis in a modular robotic system driven by a chemical programming language. *Science* **363**, eaav2211 (2019).

35. Elvira, K. S., Casadevall i Solvas, X., Wootton, R. C. R. & deMello, A. J. The past, present and potential for microfluidic reactor technology in chemical synthesis. *Nat. Chem.* **5**, 905–915 (2013).

36. Canty, R. B. & Abolhasani, M. Reproducibility in automated chemistry laboratories using computer science abstractions. *Nat. Synth.* **3**, 1327–1339 (2024).

37. Moore, J. S. & Jensen, K. F. "Batch" kinetics in flow: online IR analysis and continuous control. *Angew. Chem. Int. Ed.* **53**, 470–473 (2014).

38. Raissi, M., Perdikaris, P. & Karniadakis, G. E. Physics-informed neural networks: a deep learning framework for solving forward and inverse problems involving nonlinear partial differential equations. *J. Comput. Phys.* **378**, 686–707 (2019).

39. Karniadakis, G. E. *et al.* Physics-informed machine learning. *Nat. Rev. Phys.* **3**, 422–440 (2021).

40. Ji, W., Qiu, W., Shi, Z., Pan, S. & Deng, S. Stiff-PINN: physics-informed neural network for stiff chemical kinetics. *J. Phys. Chem. A* **125**, 8098–8106 (2021).

41. Hessel, V., Hardt, S. & Löwe, H. *Chemical Micro Process Engineering: Fundamentals, Modelling and Reactions*. (Wiley-VCH, Weinheim, 2004).

42. Kockmann, N. *Transport Phenomena in Micro Process Engineering*. (Springer, Berlin, Heidelberg, 2008).

43. Kockmann, N., Thenée, P., Fleischer-Trebes, C., Laudadio, G. & Noël, T. Safety assessment in development and operation of modular continuous-flow processes. *React. Chem. Eng.* **2**, 258–280 (2017).

44. Lin, C.-P. & Tseng, J.-M. Green technology for improving process manufacturing design and storage management of organic peroxide. *Chem. Eng. J.* **180**, 284–292 (2012).

45. Koscher, B. A. *et al.* Autonomous, multiproperty-driven molecular discovery: from predictions to measurements and back. *Science* **382**, eadi1407 (2023).

46. Lowe, D. Chemical reactions from US patents (1976-Sep2016). figshare https://doi.org/10.6084/m9.figshare.5104873.v1 (2017).

47. Chung, Y. G. *et al.* Advances, updates, and analytics for the computation-ready, experimental metal–organic framework database: CoRE MOF 2019. *J. Chem. Eng. Data* **64**, 5985–5998 (2019).

48. Jain, A. *et al.* Commentary: The Materials Project: A materials genome approach to accelerating materials innovation. *APL Mater.* **1**, 011002 (2013).

49. Winther, K. T. *et al.* Catalysis-Hub.org, an open electronic structure database for surface reactions. *Sci. Data* **6**, 75 (2019).

50. Chanussot, L. *et al.* Open Catalyst 2020 (OC20) dataset and community challenges. *ACS Catal.* **11**, 6059–6072 (2021).

51. Rosen, A. S. *et al.* Machine learning the quantum-chemical properties of metal–organic frameworks for accelerated materials discovery. *Matter* **4**, 1578–1597 (2021).

52. Hachmann, J. *et al.* The Harvard Clean Energy Project: large-scale computational screening and design of organic photovoltaics on the World Community Grid. *J. Phys. Chem. Lett.* **2**, 2241–2251 (2011).

53. Schwaller, P. *et al.* Mapping the space of chemical reactions using attention-based neural networks. *Nat. Mach. Intell.* **3**, 144–152 (2021).

54. van der Maaten, L. & Hinton, G. Visualizing data using t-SNE. *J. Mach. Learn. Res.* **9**, 2579–2605 (2008).

55. Dobbelaere, M. R., Lengyel, I., Stevens, C. V. & Van Geem, K. M. Rxn-INSIGHT: fast chemical reaction analysis using bond-electron matrices. *J. Cheminform.* **16**, 37 (2024).

56. Dagdelen, J. *et al.* Structured information extraction from scientific text with large language models. *Nat. Commun.* **15**, 1418 (2024).

57. Zheng, L. *et al.* Judging LLM-as-a-judge with MT-Bench and Chatbot Arena. in *Advances in Neural Information Processing Systems* (eds Oh, A. et al.) vol. 36 46595–46623 (Curran Associates, Inc., 2023).

58. Schwaab, M. & Pinto, J. C. Optimum reference temperature for reparameterization of the Arrhenius equation. Part 1: Problems involving one kinetic constant. *Chem. Eng. Sci.* **62**, 2750–2764 (2007).

59. Froment, G. F., Bischoff, K. B. & De Wilde, J. *Chemical Reactor Analysis and Design*. (Wiley, Hoboken, 2011).

60. Zhao, K. EchoChemAI. https://www.echochemai.cn/.

61. Han, Y. *et al.* Atomically dispersed Pd-Mn dual-metal doped CeO_2 nanorods for efficient methane oxychlorination. *Nat. Commun.* **17**, 1339 (2026).

62. ecoinvent. ecoinvent database 3.10. https://ecoinvent.org/database/ (2023).

63. Shanghai HiQ Smart Data Co., Ltd. HiQLCD database 1.2.0. https://hiq.earth (2025).

Acknowledgments

Funding:

National Key R&D Program of China grant 2022ZD0117501 (X.W.)

Scientific Research Innovation Capability Support Project for Young Faculty grant ZYGXQNJSKYCXNLZCXM-E7 (X.W.)

Tsinghua University Initiative Scientific Research Program and China Petroleum & Chemical Corporation grant 223243 (X.W.)

Author information

Authors and Affiliations

Beijing Key Laboratory of Artificial Intelligence for Advanced Chemical Engineering Materials, State Key Laboratory of Chemical Engineering and Low-Carbon Technology, Department of Chemical Engineering, Tsinghua University, Beijing 100084, China

Zemeng Wang, Wentao Li, Ruixuan Chen, Kai Zhao, Jiangjie Qiu & Xiaonan Wang

State Key Laboratory of Chemical Engineering and Low-Carbon Technology, Department of Chemical Engineering, Tsinghua University, Beijing 100084, China

Tian Yang, Zhuo Chen & Jianhong Xu

Department of Biotechnology & Enzyme Catalysis, Institute of Biochemistry, University of Greifswald, Greifswald 17487, Germany

Manu Suvarna

Contributions

X.W. conceptualized the study. Z.W. curated the data. Z.W. and W.L. developed the methodology. T.Y. designed the automated instrumentation and acquired the experimental data. K.Z. supported the life cycle assessment. Z.C. and J.X. provided the experimental facilities. Z.W. and W.L. prepared the original draft. R.C., J.Q., M.S., Z.C. and J.X. reviewed and edited the manuscript.

Corresponding authors

Correspondence to Xiaonan Wang, Jianhong Xu or Zhuo Chen.

Ethics declarations

Competing interests

The authors declare no competing interests.

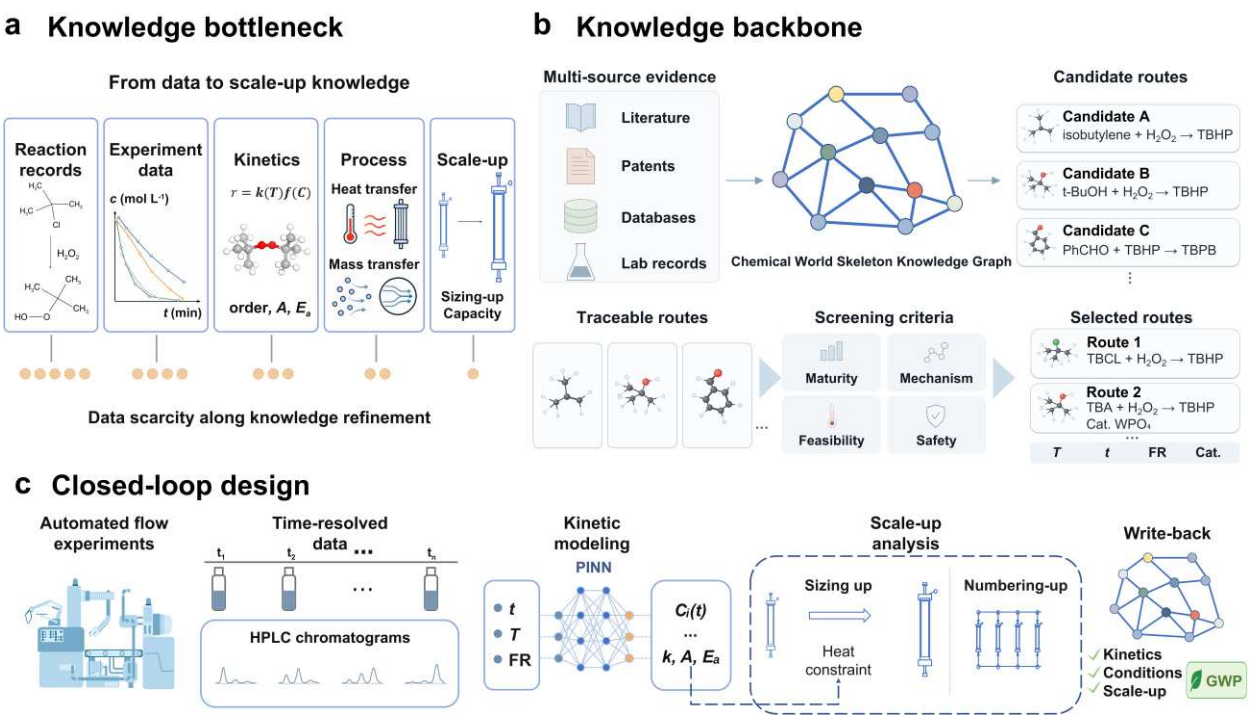


Fig. 1 | A knowledge-intensified closed loop for reaction and process development. a, Conceptual progression from reaction records to time-resolved data, kinetic descriptions, transport constraints and scale-up knowledge. The declining number of dots illustrates information scarcity. **b,** Integration of literature, patents, databases and laboratory records into the Chemical World Skeleton Knowledge Graph (CWSKG), followed by retrieval and screening of candidate routes for automated flow experiments. **c,** Coupling of automated flow experiments, concentration data, PINN–ODE kinetic modeling, reactor-scale analysis and knowledge write-back for subsequent retrieval and reuse.

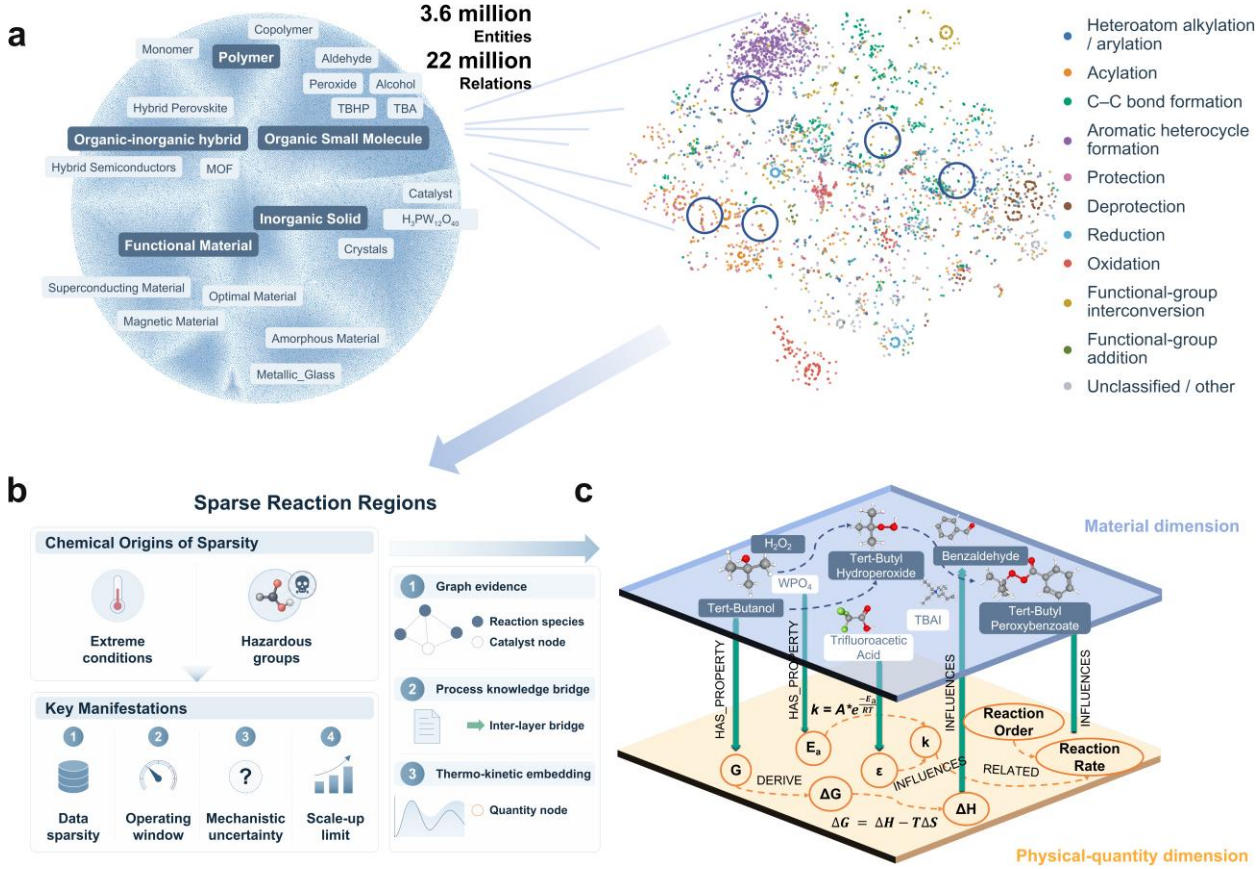


Fig. 2 | Chemical knowledge coverage and the dual-dimensional CWSKG representation. a, Graph overview and an unsupervised t-distributed stochastic neighbor embedding (t-SNE) map of reaction-center fingerprints for a reaction subset derived from United States Patent and Trademark Office (USPTO) data. Colors denote ten reaction classes and an unclassified group. Blue circles indicate regions with sparse reaction data. **b,** Chemical factors associated with sparse reaction evidence, gaps in operating conditions, mechanism and scale-up knowledge, and their linkage to graph and physical-quantity representations. **c,** Material entities linked to physical quantities through typed bridge relations, with additional relations between quantities. The lower layer represents thermodynamic and kinetic descriptors, including Gibbs free energy, enthalpy, activation energy, rate coefficients and reaction orders.

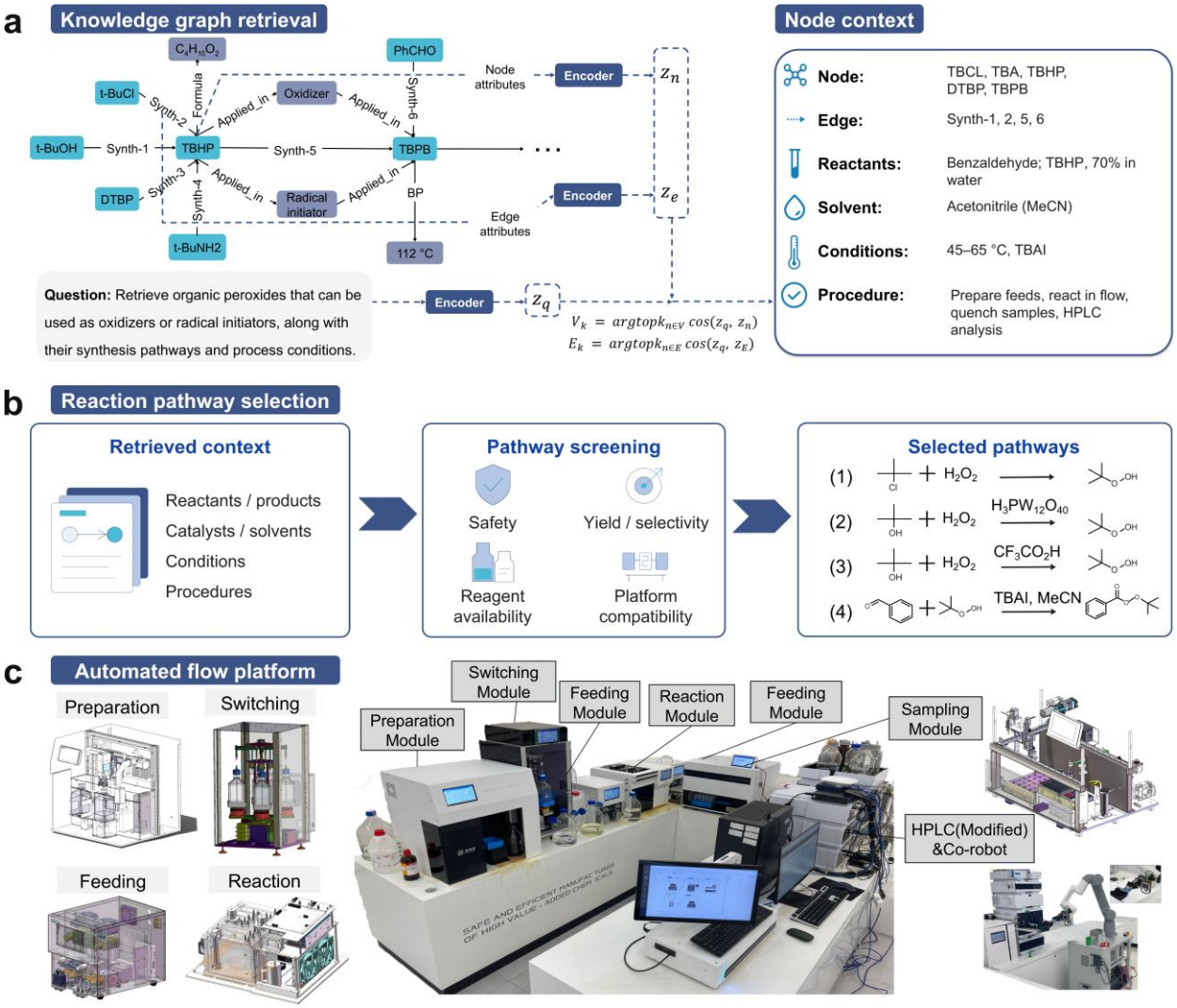


Fig. 3 | Graph retrieval and translation of selected peroxide routes into flow experiments. a, Query-guided retrieval of node and edge attributes and their assembly into a structured context. **b,** Screening of retrieved pathways against safety, yield/selectivity, reagent availability and platform compatibility, yielding the four investigated routes. **c,** Platform photograph and module views showing preparation, switching, feeding, reaction, sampling and chromatographic analysis with robot-assisted handling. Routes 1–3 target tert-butyl hydroperoxide (TBHP); Route 4 targets tert-butyl peroxybenzoate (TBPB). DTBP, di-tert-butyl peroxide; HPLC, high-performance liquid chromatography; TBAI, tetrabutylammonium iodide; MeCN, acetonitrile. BP, boiling point.

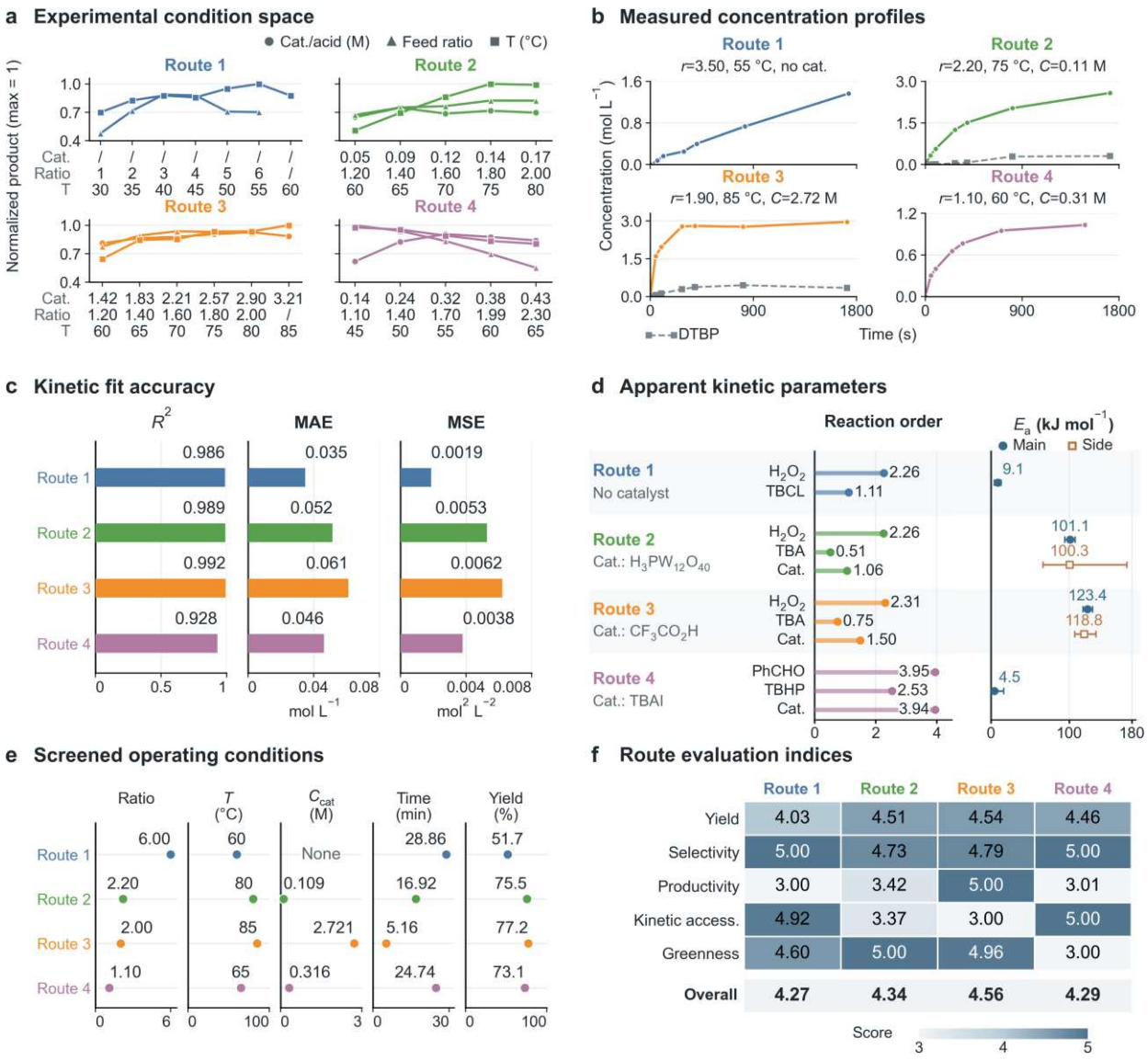


Fig. 4 | Experimental responses, kinetic fits and model-based route evaluation. a, Peak product concentrations across catalyst/acid concentration, feed-ratio and temperature scans, with each curve normalized to the maximum concentration for its route. **b,** Product concentration–time profiles for the condition family with the highest experimentally measured product concentration in each route. Gray dashed lines show di-tert-butyl peroxide (DTBP) in Routes 2 and 3. **c,** Model prediction metrics for the fitted product-concentration data evaluated on the six non-initial observations per condition: coefficient of determination (R^2), mean absolute error (MAE) and mean squared error (MSE). **d,** Catalysts, species-labeled apparent main-reaction orders and activation energies E_a for the represented main and side reactions. Error bars indicate 95% confidence intervals. **e,** Model-selected optimal feed ratios, temperatures, catalyst concentrations and residence times, with the corresponding predicted product yields. **f,** Dimensionless route scores (3–5; higher is preferred) for yield, model-defined selectivity, productivity, kinetic accessibility and scenario-based greenness assessed using global warming potential (GWP). Kinetic accessibility uses main-reaction E_a; Overall is the weighted composite. Cat./cat., catalyst or acid; C and C_{cat}, catalyst or acid concentration; T, reaction temperature; M, mol L^{-1}; r and Ratio, feed molar ratio.

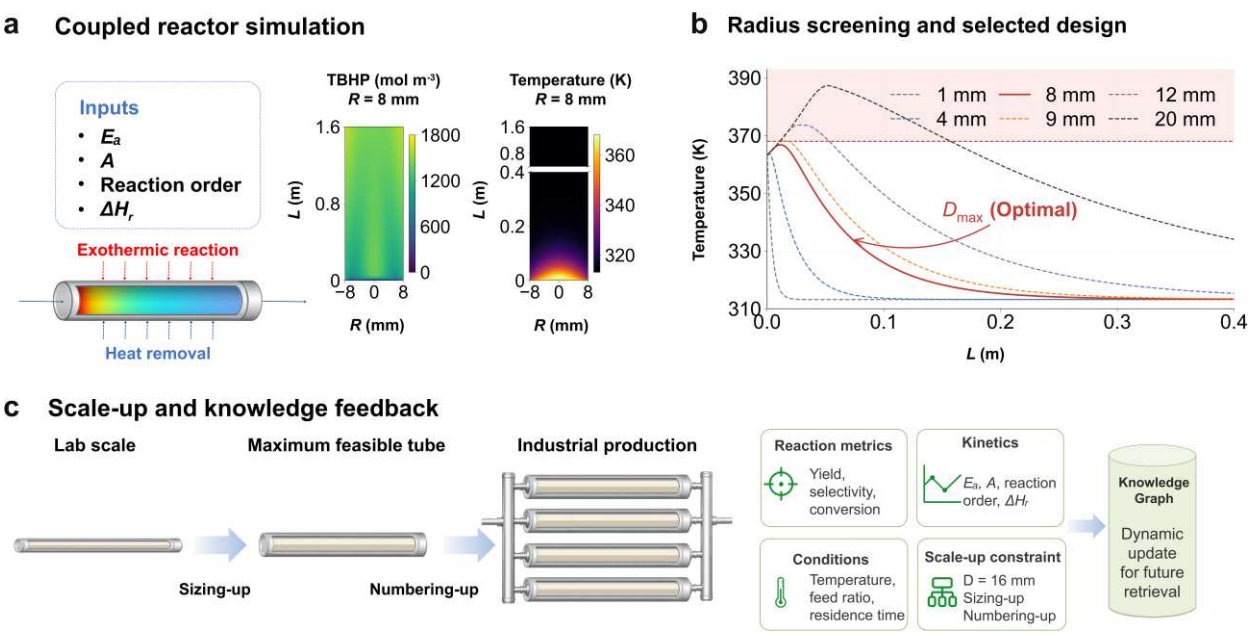


Fig. 5 | Thermal constraints on tubular-reactor scale-up and knowledge feedback. a, Coupling of reaction kinetics, heat generation and transport in a two-dimensional axisymmetric model of Route 2, with TBHP concentration and temperature fields at tube radius $R = 8$ mm. The temperature map uses different axial scales below and above $L = 0.4$ m. **b,** Centerline temperature profiles over the first 0.4 m for selected tube radii relative to the 368 K thermal-screening criterion. The 8 mm case (D_{max} = 16 mm) is the largest tested radius satisfying this model criterion, with a peak temperature of 366.7 K. **c,** Conceptual progression from single-tube enlargement to numbering-up and write-back of reaction metrics, kinetic descriptors, operating conditions and scale-up constraints to the knowledge graph for subsequent retrieval.

Supplementary Files

This is a list of supplementary files associated with this preprint. Click to download.

- SupplementaryData.zip
- KIcLoopSI.docx